IOP Publishing Journal of Physics D: Applied Physics
J. Phys. D: Appl. Phys. **55** (2022) 345501 (13pp) https://doi.org/10.1088/1361-6463/ac7365

Three-dimensional mathematical modelling and dynamic analysis of freestanding triboelectric nanogenerators

Xin Guo[1,2,5], Jiajia Shao[1,2,5], Morten Willatzen[1,2], Yi Yang[3] and Zhong Lin Wang[1,2,4,*]

[1] Beijing Institute of Nanoenergy and Nanosystems, Chinese Academy of Sciences, Beijing 101400, People's Republic of China
[2] School of Nanoscience and Technology, University of Chinese Academy of Sciences, Beijing 100049, People's Republic of China
[3] Research Laboratory of Electronics, Massachusetts Institute of Technology, Cambridge, MA, United States of America
[4] School of Materials Science and Engineering, Georgia Institute of Technology, Atlanta, GA 30332-0245, United States of America

E-mail: zlwang@gatech.edu

Received 29 March 2022, revised 13 May 2022
Accepted for publication 24 May 2022
Published 7 June 2022

Abstract

Energy harvesting system based on triboelectric nanogenerators (TENGs) has aroused wide interest from many researchers since it integrates multiple disciplines together including electromagnetics, electric circuit theory, materials science and mechanical engineering. Accurate modeling of a TENG is an indispensable part for revealing the relationships and interactions among physical quantities from different areas. Here, a three-dimensional mathematical model of a contact-mode freestanding TENGs (CF-TENGs) is built with a combination of physical abstraction and geometry configuration, which makes it possible to dynamically analyze the variations of the field and circuit quantities. An accurate Norton's equivalent circuit model that consists of a current source in parallel with a pure capacitive reactance is proposed. Based on this model the reason for identifying the displacement current as the driving force of TENGs is elucidated, and quantitatively determine the current flowing through the external load resistor and the internal equivalent capacitor. More importantly, a universal dynamic simulation model consisting of a quasi-electrostatic model and a circuit model for the TENG-based energy harvesting system is presented. The presented composite model exhibits an obvious advantage in terms of revealing the dynamic output of TENGs with arbitrary geometry and charge distribution. Finally, based on the characteristics of linearity and time-invariance of the CF-TENG, general optimization strategies are pinpointed, which allow us to accurately predict the maximum output efficiency (close to 82.5%).

[5] These authors contributed equally to this work.
[*] Author to whom any correspondence should be addressed.

Supplementary material for this article is available online

Keywords: freestanding triboelectric nanogenerators, three-dimensional mathematical model, displacement current, dynamic simulation model, energy harvesting system

(Some figures may appear in colour only in the online journal)

1. Introduction

The movement and redistribution of charges in a TENG device result in the time-varying electric field and polarization of the dielectric material, which are essential factors that affect the output performance of an energy harvesting system [1–6]. System models, as an extraction and abstraction of reality, are usually built to reveal and predict the full details of charge flow. The characteristics of the built model is that some, but not all, features of the real system are reflected in the model. Till now, there are two categories for which theoretical models have been established for a TENG device: equivalent electrical circuit models and physical-based models [7–10]. The first category includes the capacitive model and Norton's equivalent circuit model according to the first order of lumped parameter equivalent circuit theory [7, 9–11]; while the second category model is a quasi-electrostatic model based on Maxwell's equations [8, 9, 12–14]. It is worth highlighting that the equivalent circuit model is a new layer of abstraction on top of Maxwell's equations which is simple and easy to apply in engineering [9, 15]. According to the previously published Norton's circuit model, the TENG device is represented as a combination of a time-varying current source and TENG impedance [9, 15]. Although this model can be utilized to estimate the impedance behavior of the TENG, it cannot reflect the phase shifts of the output signals, mainly because a TENG device exhibits the characteristics of capacitive reactance due to its capacitor structure. Through the physical model, the basic physical quantities such as the time-variant electric field, polarization, electric displacement, electric flux, and displacement current, etc, can be determined which allows us to clarify the physical mechanism of TENGs.

Another type of model, commonly referred to as a mathematical model, which utilizes approaches and knowledge of mathematics to solve practical problems. Although this model may seem more abstract than a physical model, there are strong similarities between physical and mathematical models [4, 16, 17]. Generally, mathematical models have strong universal applicability and can be easily realized to quantitatively study the interactions among model variables rather than just the component parts. For instance, many models have been successfully designed and created for static or steady-state operation, where variables remain constant in time [3, 18]. However, dynamic systems, whose behavior as a function of time matches actual circumstances better, are important [19, 20]. Although a dynamic analysis is more complex than that of the static analysis, conclusions and decisions based on dynamic model can help one avoid making errors without consideration of time-varying coefficients. The geometry structure of a CF-TENG possesses excellent symmetry, what makes it different is that this type of TENG carries some specific features [21–23]. For instance, the CF-TENG-based energy harvesting system is a linear and time-invariant system because of the time-invariant inherent capacitance of the CF-TENG [21, 24]. And this characteristic makes the CF-TENG is unique when compared to other basic modes of TENGs [25]. Besides, the optimization of energy conversion systems is crucial for the wide range of applications, which can be conducted from the optimal design of the external electrical circuit, geometrical parameters and the micro- and nanostructures of materials [3, 26, 27]. However, understanding thoroughly and quantitatively the energy conversion process of the CF-TENG-based system depends on the accuracy and stability of the dynamic model, which, unfortunately, is beyond the reach of existing models and methods.

In this work, a time-dependent and three-dimensional mathematical (3D) model for CF-TENGs based on Maxwell's equations is built. Its accuracy and precision are verified by comparison with the previously published capacitive (CA) model and finite element method (FEM) model. For the first time, the relationships between transferred charges, electric flux and displacement current are elucidated. Then, according to lumped parameter circuit theory, a more accurate and intuitive Norton's equivalent circuit model is reconstructed. A general TENG device can be modeled as a current source in parallel with a pure capacitive reactance by which its capacitive characteristics are discussed in detail using the harmonic analysis method. In this way, it is possible to identify why the displacement current is the driving force of TENGs. In order to predict the dynamic output performances of TENGs with arbitrary geometric constructions and charge distributions, a multi-physics dynamic simulation model has been proposed. Using the coupled model, not only the linearity and time-invariance characteristics of the CF-TENG for different mechanical excitations are demonstrated, but also how the air gap, load resistance, and the operation frequency affect the dynamic output are confirmed and the optimization strategy for TENGs to reach the best possible design for engineering applications is outlined.

2. General theory

2.1. Mathematical modelling of the contact mode freestanding triboelectric nanogenerator

According to classical electrodynamics, charges and currents are sources for the electromagnetic field. The charge

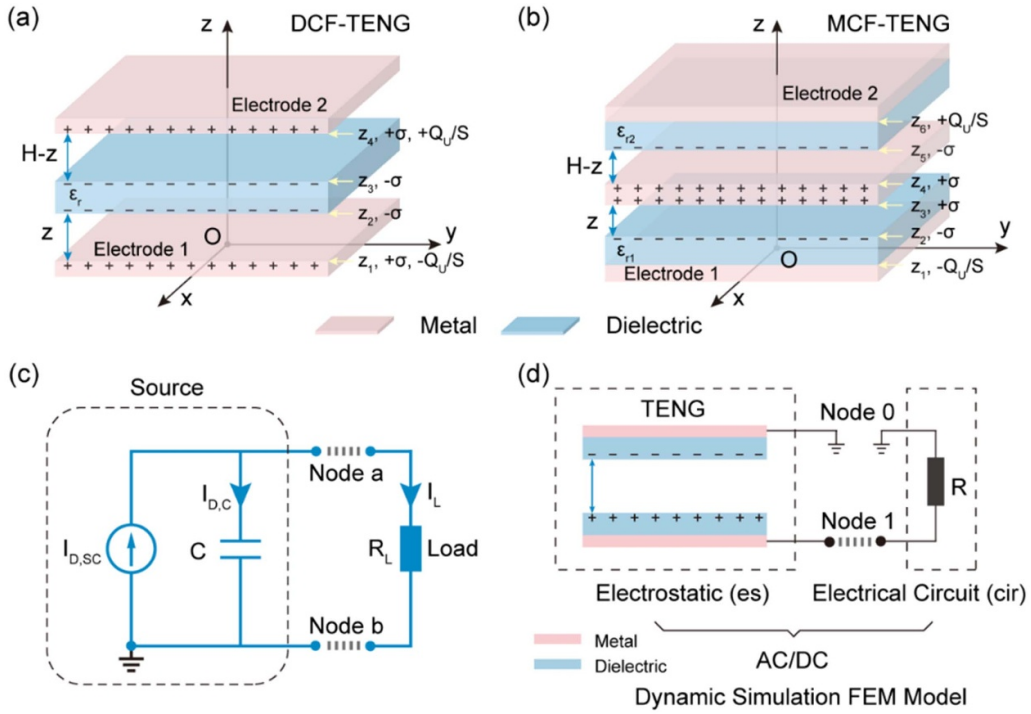

Figure 1. Theoretical models of CF-TENGs. (a), (b) Three-dimensional mathematical models of a typical dielectric layer CF-TENG (DCF-TENG) and a typical metal layer CF-TENG (MCF-TENG). (c) Norton's equivalent circuit model of a TENG device. (d) A universal dynamic simulation model for the TENG-based energy harvesting system, this multi-physics field model couples the quasi-electrostatic mode and electrical circuit together.

distribution and movement can directly affect the quasi-electric field distributions of TENGs. Although magnetic fields curl around moving charges (currents), it is really quite negligible because of the low operation frequency of TENGs triggered by external mechanical excitation. Here, the studies are based on two assumptions: (a) the charges are distributed uniformly on the contacting surfaces and electrodes when a TENG works under a dynamic equilibrium; (b) the magnetic field of moved charges is extremely small, thus it is negligible in our work.

There are two typical CF-TENGs depicted in figures 1(a) and (b), respectively: the dielectric-freestanding-layer CF-TENG (DCF-TENG) and the metal-freestanding-layer CF-TENG (MCF-TENG) with detailed configuration parameters. They are constructed from freely moving parts. The movable part of the former is the dielectric material, while for the latter it is the metal layer. Considering figure 1(a) as an example, there are four charged surfaces: the two tribo-charged surfaces ($\pm\sigma$) are generated on the dielectric surfaces and they are constant in time and the other two charged layers ($\pm Q_U/S$) are distributed on the electrodes which are time-varying due to the movement of the freestanding dielectric material. For the same reason, the MCF-TENG can be modeled as six charged surfaces (figure 1(b)), where two of them are time-varying while the dielectric surfaces are time-invariant. Free charges are transferred between the two electrodes, resulting in a time-varying electric field distribution and material polarization thereby affecting the output behavior in the external circuit. Six different geometry configurations of CF-TENGs are designed (supplementary figure S1 (available online at stacks.iop.org/JPhysD/55/345501/mmedia)), to help understand the distribution of charges. It can be easily observed that vertically symmetric structures lead to vertical symmetry of charge distributions.

On the other hand, electromagnetic theories are generally universal and have remained unchanged since the beginning of time when they were found. For instance, the electric filed is functions of time and space coordinates and its variation rules do not change even at different coordinate system. And most of the time the interaction between model variables can be clarified conveniently and clearly, since one could evaluate influences of input variables on output parameters quantitatively. Therefore, a time-dependent and three-dimensional mathematical model for the CF-TENG can be established, according to the above assumptions (supplementary note 1). Solving the Poisson equation, the electric potential and spatial distribution of the electric field determined by charge distributions can be derived theoretically (supplementary note 1). Note that this is a common way that is applicable to other relevant quasi-electrostatics. For the MCF-TENG with special uniformly charge distributions, its electric potential ϕ (0, 0, *z, t*) having a vertical symmetry axis is given by applying Coulomb's law (supplementary note 2)

$$\phi(0,0,z,t) = -\frac{Q_{\mathrm{U}}}{4\pi\varepsilon_0 S}\int_{-\frac{W}{2}}^{\frac{W}{2}}\int_{-\frac{L}{2}}^{\frac{L}{2}}\frac{dx'dy'}{\left[x'^2+y'^2+(z-z_1)^2\right]^{1/2}} + \frac{\sigma}{4\pi\varepsilon_0}\int_{-\frac{W}{2}}^{\frac{W}{2}}\int_{-\frac{L}{2}}^{\frac{L}{2}}\frac{dx'dy'}{\left[x'^2+y'^2+(z-z_1)^2\right]^{1/2}} - \frac{\sigma}{4\pi\varepsilon_0}\int_{-\frac{W}{2}}^{\frac{W}{2}}\int_{-\frac{L}{2}}^{\frac{L}{2}}\frac{dx'dy'}{\left[x'^2+y'^2+(z-z_2)^2\right]^{1/2}} - \frac{\sigma}{4\pi\varepsilon_0}\int_{-\frac{W}{2}}^{\frac{W}{2}}\int_{-\frac{L}{2}}^{\frac{L}{2}}\frac{dx'dy'}{\left[x'^2+y'^2+(z-z_3)^2\right]^{1/2}} + \frac{\sigma}{4\pi\varepsilon_0}\int_{-\frac{W}{2}}^{\frac{W}{2}}\int_{-\frac{L}{2}}^{\frac{L}{2}}\frac{dx'dy'}{\left[x'^2+y'^2+(z-z_4)^2\right]^{1/2}} + \frac{Q_{\mathrm{U}}}{4\pi\varepsilon_0 S}\int_{-\frac{W}{2}}^{\frac{W}{2}}\int_{-\frac{L}{2}}^{\frac{L}{2}}\frac{dx'dy'}{\left[x'^2+y'^2+(z-z_4)^2\right]^{1/2}} \tag{1}$$

where σ represents the tribo-charge density and Q_{U} the transferred charges. W and L are the width and length of the electrodes, respectively; and the corresponding area is represented by S. The dimensions of the freely moving part is of the same as that of the electrode. The notions z_1, z_2, z_3, and z_4 denote the z-coordinates of the upper surface of the lower electrode sheet, the lower surface of the dielectric, the upper surface of the dielectric, and the lower surface of the upper electrode sheet, respectively, where z_2 and z_3 are time-dependent variables (figures 1(a) and (b)).

Subject to open-circuit (OC) boundary condition, no charges are transferred between the electrodes so that the term Q_{U} is set to zero. The voltage at OC condition is given by $V_{\mathrm{OC}} = \phi_1(0,0,z_1,t) - \phi_2(0,0,z_4,t)$. Because of the equivalent electric potential at short-circuit (SC) conditions, we get the equation $\phi_1(0,0,z_1,t) = \phi_2(0,0,z_4,t)$, from which the transferred charge and corresponding conductive current can be obtained. If an external resistor Z_{L} is connected between the two electrodes, based on Kirchhoff's voltage law, a first-order differential equation with respect to time is obtained

$$-Z_{\mathrm{L}}\frac{\mathrm{d}Q_{\mathrm{U}}}{\mathrm{d}t} = \phi_1(0,0,z_1,t) - \phi_2(0,0,z_4,t) \tag{2}$$

where ϕ_1 (0, 0, z_1, t), and ϕ_2 (0, 0, z_4, t) represent the electric potential of the electrode 1, and electrode 2, respectively; and their expressions are shown in supplementary note 2. Observe that equation (2) is the governing equation for the CF-TENG, and by solving it, the time-varying transferred charges under various loading conditions can be determined. Furthermore, the time-varying variables such as the electric field, electric flux, electric displacement, etc, for the internal circuit, or (the time-varying current, voltage, power, etc) from the external circuit can be calculated. In other words, mathematical modeling makes it possible to dynamically analyze the output performance of the CF-TENG energy harvesting system. Through the same method, the equations for describing the basic outputs of a typical MCF-TENG (figure 1(b)) are derived, the details of which are demonstrated in supplementary note 3.

2.2. Norton's equivalent circuit model

Norton's equivalent circuit model of the TENG device has been proposed based on the lumped parameter circuit theory, from which a TENG is equivalent to a combination of a time variant current source and an internal impedance [9, 12]. However, due to the introduction of an internal impedance, the conduction current following through the external load is in phase with the current source I_{N}, which does not reflect the real output characteristics of TENG devices [9, 12]. What is at the bottom of cause is the basic structure of capacitive of TENGs, and therefore Norton's equivalent circuit model of a TENG should be consisted of a current source in parallel with a pure capacitive reactance. For the DCF-TENG, its current source I_{N} and equivalent capacitance C_{eff} are given by (supplementary note 6):

$$I_{\mathrm{N}}(t) = I_{\mathrm{SC}}(t) = S\sigma\frac{\mathrm{d}}{\mathrm{d}t}\frac{(M_{24}+M_{34})-(M_{21}+M_{31})}{2(M_{11}-M_{41})} \tag{3}$$

$$C_{\mathrm{eff}} = \frac{S}{2(M_{11}-M_{14})} \tag{4}$$

where

$$M_{ij} = \frac{1}{4\pi\varepsilon_0}\int_{-\frac{W}{2}}^{\frac{W}{2}}\int_{-\frac{L}{2}}^{\frac{L}{2}}\frac{\mathrm{d}x'\mathrm{d}y'}{\left[x'^2+y'^2+(z_j-z_i)^2\right]^{1/2}} \tag{5}$$

where M_{ij} represents the electric potential at $(0, 0, z_j)$ produced by a charge plane which is parallel with x–y plane and locates at $z = z_i$ with charge density of 1 C m^{-2}, and i and j represent the positive integers in the set (1, 2, 3, 4), respectively.

When an external resistor R_{L} is connected, the current generated by the TENGs will be divided into two contributions (figure 1(c)): the first contribution passes through the internal equivalent capacitor of the TENG device, while the second contribution flows into the external circuit or flows into the external resistance. Based on Kirchhoff's current law (KCL) and the voltage-current relationship of circuit elements, the current source I_{N} is determined by the following differential equation:

$$I_{\mathrm{L}} + R_{\mathrm{L}}\frac{\mathrm{d}(I_{\mathrm{L}}C_{\mathrm{eff}})}{\mathrm{d}t} = I_{\mathrm{N}} \tag{6}$$

$$I_{\mathrm{D,C}} = R_{\mathrm{L}}\frac{\mathrm{d}(I_{\mathrm{L}}C_{\mathrm{eff}})}{\mathrm{d}t} \tag{7}$$

where I_{L} and $I_{\mathrm{D,C}}$ represent the current flowing through the load resistor and the internal equivalent capacitor, respectively. Since the output signals of the TENG are not sinusoidal, it is difficult to obtain analytical solutions directly. However, since the TENG's equivalent circuit is a linear circuit, it allows us to exploit the principle of superposition to solve the above

problem in a simple and clear way [28]. In fact, the current source I_N is a discrete-time periodic signal sequence (written as a periodic sequence $x[n]$ with fundamental period N [24]), whose discrete-time Fourier series coefficients a_k are given by:

$$a_k = \frac{1}{N}\sum_{n=\langle N\rangle} x[n]\, e^{-jk\omega_0 n} = \frac{1}{N}\sum_{n=\langle N\rangle} x[n]\, e^{-jk(2\pi/N)n} \tag{8}$$

where j is the imaginary unit, k ranges over a set of N successive integers, and $\omega_0 = 2\pi/N$ is the fundamental frequency. These coefficients a_k specify the decomposition of the given $x[n]$ into the sum of N harmonically related complex exponentials through the following equation [24]:

$$x[n] = \sum_{k=\langle N\rangle} a_k e^{jk\omega_0 n} = \sum_{k=\langle N\rangle} a_k e^{jk(2\pi/N)n}. \tag{9}$$

Solving the KCL equations of a circuit is a useful approach to get the response for any excitation signal. For the Norton circuit of CF-TENGs whose equivalent capacitance is time-invariant with a sinusoidal excitation, equation (6) is rewritten as:

$$I_L + R_L C_{eff}\frac{dI_L}{dt} = I_{Nm}\cos(\omega t + \psi_N) \tag{10}$$

where I_{Nm}, ω and ψ_N are the amplitude, frequency and phase angle of the sinusoidal signal, respectively. The corresponding solution is the sum of the general solution (I_{Lh}) expressed as an exponentially decaying function in addition to the particular solution (I_{Lp}), which behaves as a sinusoidal time function with the same frequency as the external excitation:

$$I_L(t) = I_{Lh}(t) + I_{Lp}(t) = Ke^{-\frac{t}{R_L C_{eff}}} + I_{Lm}\cos(\omega t + \psi_L) \tag{11}$$

where I_{Lm} and ψ_L are the amplitude and phase angle of the current through the load, respectively, and which can be calculated by phasor analyzing directly:

$$I_{Lm} = \frac{I_{Nm}/R_L}{\sqrt{(\omega C_{eff})^2 + \left(\frac{1}{R_L}\right)^2}} \tag{12a}$$

$$\psi_L = \psi_N - \arctan(\omega R_L C_{eff}). \tag{12b}$$

In additional, K is an undetermined coefficient related with initial condition, generally written as:

$$K = I_L(0) - I_{Lm}\cos(\psi_L). \tag{13}$$

It is also critical to determine the generation and variation of the current source I_N. According to our previously published works, it is known that the displacement current is regarded as the driving force of TENGs. For the CF-TENG, the displacement current in the z-direction ($I_{D,z}$) is given by (supplementary note 2):

$$\begin{aligned}
I_{D,z}(z,t) &= \int_S \frac{\partial \boldsymbol{D}}{\partial t}\cdot \boldsymbol{n} dS \\
&= -\frac{z-z_1}{4\pi S}\frac{\partial}{\partial t}\left\{Q_U\int_{-\infty}^{\infty}\int_{-\infty}^{\infty} dxdy\int_{-\frac{W}{2}}^{\frac{W}{2}}\int_{-\frac{L}{2}}^{\frac{L}{2}}\frac{dx'dy'}{\left[(x'-x)^2+(y'-y)^2+(z-z_1)^2\right]^{3/2}}\right\} \\
&\quad + \frac{\sigma(z-z_1)}{4\pi}\frac{\partial}{\partial t}\left\{\int_{-\infty}^{\infty}\int_{-\infty}^{\infty} dxdy\int_{-\frac{W}{2}}^{\frac{W}{2}}\int_{-\frac{L}{2}}^{\frac{L}{2}}\frac{dx'dy'}{\left[(x'-x)^2+(y'-y)^2+(z-z_1)^2\right]^{3/2}}\right\} \\
&\quad - \frac{\sigma}{4\pi}\frac{\partial}{\partial t}\left\{(z-z_2)\int_{-\infty}^{\infty}\int_{-\infty}^{\infty} dxdy\int_{-\frac{W}{2}}^{\frac{W}{2}}\int_{-\frac{L}{2}}^{\frac{L}{2}}\frac{dx'dy'}{\left[(x'-x)^2+(y'-y)^2+(z-z_2)^2\right]^{3/2}}\right\} \\
&\quad - \frac{\sigma}{4\pi}\frac{\partial}{\partial t}\left\{(z-z_3)\int_{-\infty}^{\infty}\int_{-\infty}^{\infty} dxdy\int_{-\frac{W}{2}}^{\frac{W}{2}}\int_{-\frac{L}{2}}^{\frac{L}{2}}\frac{dx'dy'}{\left[(x'-x)^2+(y'-y)^2+(z-z_3)^2\right]^{3/2}}\right\} \\
&\quad + \frac{\sigma(z-z_4)}{4\pi}\frac{\partial}{\partial t}\left\{\int_{-\infty}^{\infty}\int_{-\infty}^{\infty} dxdy\int_{-\frac{W}{2}}^{\frac{W}{2}}\int_{-\frac{L}{2}}^{\frac{L}{2}}\frac{dx'dy'}{\left[(x'-x)^2+(y'-y)^2+(z-z_4)^2\right]^{3/2}}\right\} \\
&\quad + \frac{z-z_4}{4\pi S}\frac{\partial}{\partial t}\left\{Q_U\int_{-\infty}^{\infty}\int_{-\infty}^{\infty} dxdy\int_{-\frac{W}{2}}^{\frac{W}{2}}\int_{-\frac{L}{2}}^{\frac{L}{2}}\frac{dx'dy'}{\left[(x'-x)^2+(y'-y)^2+(z-z_4)^2\right]^{3/2}}\right\}.
\end{aligned} \tag{14}$$

Simplifying equation (14), the relationship between the displacement current and the conduction current (I_L) that flows through the external resistance R_L can be obtained, which is (supplementary note 6):

$$I_D = \int_S \frac{\partial \mathbf{D}}{\partial t} \cdot \mathbf{n} dS = -\frac{dQ_U}{dt} = -I_L. \quad (15)$$

At SC conditions, all the charges will be transferred in the external circuit; therefore, the following equation in combination with equation (3) is obtained:

$$I_N(t) = I_{SC}(t) = -I_{D,SC}(t). \quad (16)$$

This equation implies that $I_{D,SC}$ is equivalent to the current source I_N but of opposite direction, which verifies our previous conclusion. Evidently, the circuit theory obtained here reflects Maxwell's equations for the application of the dynamic electromagnetic theory to practical engineering [4].

2.3. Dynamic simulation model

Although a dynamic model is more complex than a static model, the former reflects a practical situation better. For TENGs, the most common approach has been built through a static physical model using COMSOL software with the FEM [29, 30]. There is no denying that using the quasi-static model the spatial characteristics of the electric potential, electric field, and charge distribution can be calculated easily, but it is suitable only for calculating the transferred charges at SC condition (Q_{SC}) and potential difference at OC condition (V_{OC}), which do not suffice to analyze dynamic situations, such as observing the time-varying charge transfers between the two electrodes of TENGs. A dynamic simulation model of TENGs is built through the COMSOL Multiphysics software, which is composed of the electrostatic interface, and electrical circuit interface in the AC/DC module as well as the moving mesh interface under the mathematics module (figure 1(d)).

Taking the model depicted in figure 1(d) as an example, one electrode (such as the top electrode) of the TENG device is set as 'Ground', while the other is the 'Circuit Terminal', and both of them are connected by an external I vs. U component from electrical circuit interface so as to the output power to external circuit. On the other hand, the external I vs. U component works as a power source in circuit and an equivalent resistor representing the impedance of an external circuit is introduced. Both of the external I vs. U component, and the equivalent resistor are all double-port elements, which are connected between the Node 0 and Node 1. By the way, the motion equation must be added in the moving mesh interface to describe the external mechanical triggering.

3. Results and discussion

The corresponding numerical calculations and comparison of results from the FEM method, and CA model are demonstrated in figure 2. It should be noticed that the moving part is driven by a sinusoidal wave in all our calculations (equation (S12) in supplementary note 2), and its initial position is set at the middle point of the air gap. We find that the V_{OC} and Q_{SC} are proportional to the ratio of $\Delta z/H$ (figures 2(a) and (b)), where Δz and H represent the displacement of the freestanding layer moving in the z-direction and the thickness of air gap, respectively. As a result, the capacitance of either the DCF-TENG or MCF-TENG do not change with the variation of the moving distance (figure 2(c)). Based on the equivalent circuit models of TENGs (such as the CA model), there are three different capacitors connected in series in the DCF-TENG device; one of the capacitors come from the dielectric, while two other capacitors are formed due to the air gaps (figure 1(a)). Since the thicknesses of the dielectric layer and maximum air gap are 100 μm and 10 mm, respectively, the total capacitance of the DCF-TENG is mainly affected by the air gap. For the same reason that the maximum thickness of the air gap is extremely larger than that of the dielectric in the MCF-TENG device (figure 1(b)), the inherent capacitance of this model is nearly constant when the moving distance changes. These behaviors of the CF-TENGs lead to the linear-time-invariant dynamic characteristics, and the related essential reason will be discussed in detail in figure 5. Meanwhile, we observe significant deviations between the FEM model and CA model particularly under a large thickness air gap (the insights in figures 2(a) and (b)). This phenomenon is mainly attributed to the fact that there is a uniform electric field in the CA model when building the model.

Moreover, the thickness of the air gap indicates a strong effect on the basic output of the CF-TENG (figures 2(d)–(f)). Especially when the H is small and approaches the same order of magnitude as the thickness of the dielectric material, an obvious discrepancy in Q_{SC} occurs between the results of 3D model and FEM simulations. As stated before, the DCF-TENG is modelled as four charged layers composed of two tribo-charge surfaces and two freely charge layers distributed on the surface of electrodes. Taking equation (1) as an example, the relative dielectric constant does not appear so the effect of dielectric materials is not considered. The reason for doing this is because of the symmetric structure of the DCF-TENG and the invoked mirror imaging symmetry. When H is smaller, the effects of dielectric polarization ($\boldsymbol{P}$) on the total electric field become more and more apparent, which should not be neglected. When $\boldsymbol{P}$ is considered, the calculations of Q_{SC} and C from 3D model are very similar to those of the FEM results, as depicted from the insights in figures 2(d) and (f) (supplementary note 4). The following conclusions can be drawn: (a) the intensity of dielectric polarization at SC conditions is stronger than that under OC conditions, and it can be predicted that the connected load in the external circuit reduces the polarization. (b) The 3D mathematical model is close to the CA model if the variables in the external circuits as the H is small enough.

Knowledge of the physical variables of the TENG device is a great advantage of the 3D mathematical model. The time-dependent electric field and electric displacement of the DCF-TENG are demonstrated in figures 2(g) and (h), and K and V represent the two points distributed in the dielectric layer and air gap, respectively. Both of the z-component of electric

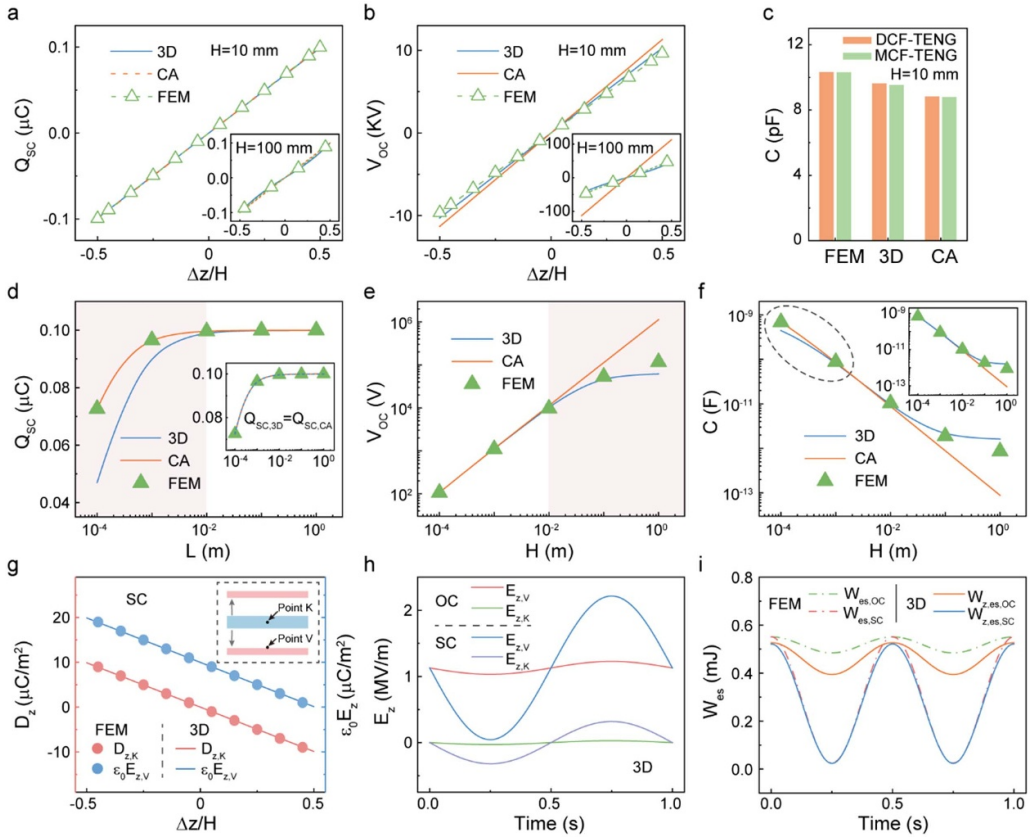

Figure 2. Results comparison of FEM simulation, 3D model and CA model for the DCF-TENG at SC, and OC conditions. (a) Transferred charges at SC condition (Q_{SC}), and (b) potential difference at OC condition (V_{OC}) with a 10 mm-thick air gap (H) with respect to the ratio of $\Delta z/H$. The insets exhibit the Q_{SC} and V_{OC} with a 100 mm-thick air gap. (c) Capacitances of the DCF-TENG and MCF-TENG with a 10 mm-thick air gap. (d) Q_{SC}, (e) V_{OC}, and (f) capacitance versus different thicknesses of air gap. (g) Variation of D_z at the point K, and E_z at the point V with respect to the ratio of $\Delta z/H$ at SC condition. (h) E_z at the point of K and V and (i) quasi-electrostatic energy with time at OC and SC conditions, respectively.

displacement (D_z) and z-component of (E_z) electric field are inversely proportional to the ratio of z/H, which means that the dielectric polarization $\boldsymbol{P}$ should also change with H (supplementary figure S3(b)). In contrast, the values of D_z decrease to zero and then increase to maximum, indicating that the direction of the electric displacement changes abrupt when the moving part moves through the middle position of the air gap. However, the direction of E_z does not change even if the intensity of E_z gradually decreases from maximum to zero. Since the tribo-charge is distributed on the contacting surfaces of the dielectric, D_z is discontinuous. The values of E_z either at the point of K or V calculated at SC conditions are larger than for OC conditions, as shown in figure 2(h). This is mainly attributed to charges transferred between the two electrodes that leads to a time-varying total electric field. It should be noticed that E_z at the K point is almost zero, illustrating that there is a negligible electric field in the dielectric under OC conditions. Furthermore, similar trends of the quasi-electrostatic energy (W_{es}) calculated by the 3D model and the FEM can be found in figure 2(i). The charge redistributions at the surface of electrode is the working principle behind the DCF-TENG.

The direction of the displacement current is closely related to the direction of the electric flux and its rate of change with time, and the latter is determined by the charges transferred between the electrodes. At SC conditions, one of the electrodes is enclosed by a 'special Gaussian surface' (the surface S_1 shown in figure 3(a)). According to Gauss's law, the electric flux (Ψ_1) passing through the surface S_1 (the outward direction is the positive direction) is equal to Q_1/ε_0, or it is easily to get the equation: $Q_1 = \varepsilon_0\Psi_1$ (Q_1: the charges distributed inside the Gaussian surface S_1). The corresponding numerical results are depicted in figure 3(b1). Besides, the change in electric flux with time ($\Delta\Psi$) is appears due to the change of Q_1 that is the transferred charge between the two electrodes (Q_U). Since charge transfer from electrode 1 to electrode 2 is set to be the positive direction, the phases of $\Delta\Psi$ and Q_U change in opposite directions (figure 3(b2)). Because of Maxwell's equations, the product of the permittivity and the change of electric flux ($\Delta\Psi$) through a surface (S_1) is the 'displacement current', even though charges do not flow through the surface. According to equation (14), the numerical calculations of $I_{D,SC}$ and I_{SC} are demonstrated in figure 3(c) as expected. A similar analysis can be found for the Gaussian surface S_2 (supplementary figure S4). As mentioned earlier, a TENG is operated at a low working frequency, and the magnetic field in the surrounding space can be neglected, so the radiation of electromagnetic waves can be discarded.

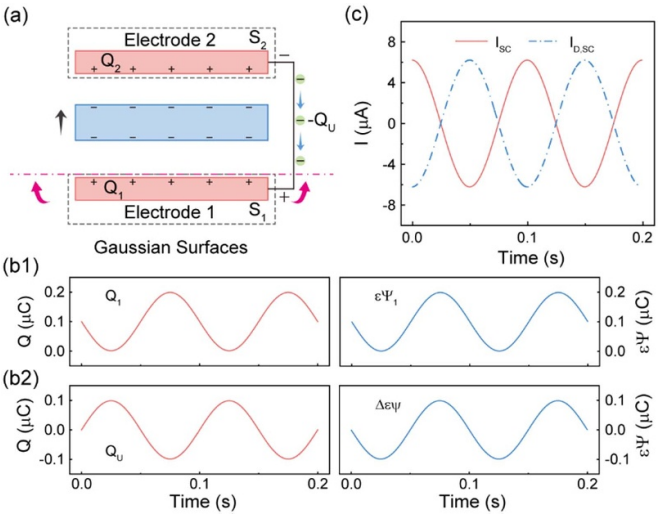

Figure 3. The electric flux, displacement current and Norton's equivalent circuit of a DCF-TENG. (a) Schematic diagram of the typical Gaussian surfaces for the DCF-TENG at SC conditions. Note that the Gaussian surface (such as S_1 and S_2) is a closed surface in three-dimensional space through which the flux of a vector field can be calculated. (b) Variations of Q_1, Ψ_1, Q_U and $\Delta\Psi$ due to the redistribution of transferred charges with respect to time. (c) The displacement current ($I_{D,SC}$) and conduction current (I_{SC})-time relationships at SC conditions.

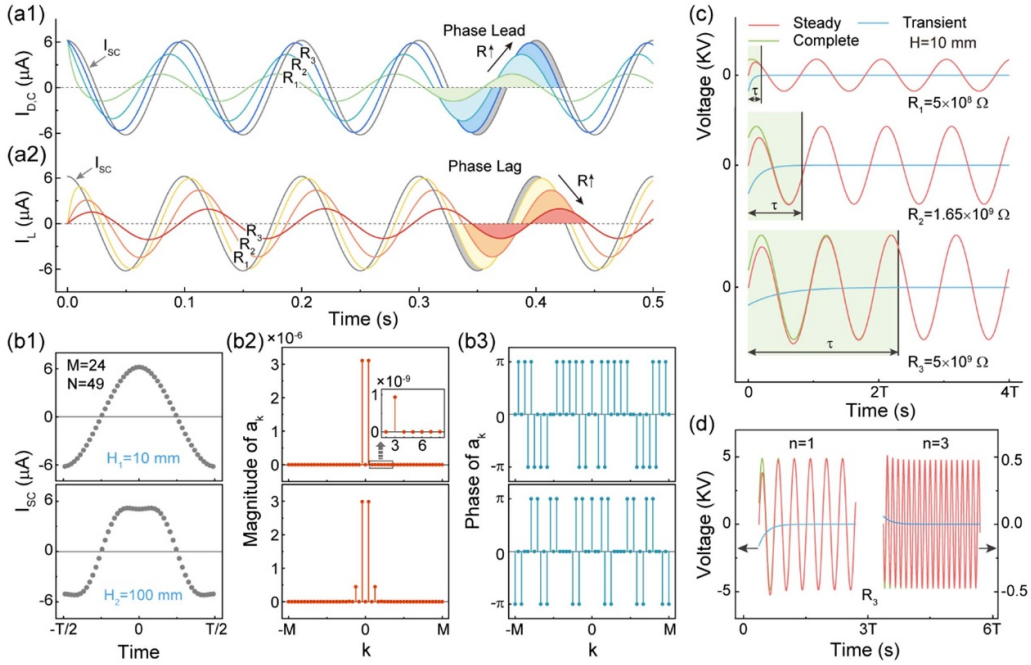

Figure 4. The basic output performances of the CF-TENG numerically calculated through the Norton's equivalent circuit model. (a) The current passing through the TENG device ($I_{D,C}$) and the external resistor (I_L) under three different loading conditions ($R_1 = 5 \times 10^8$ Ω, $R_2 = 1.65 \times 10^9$ Ω, $R_3 = 5 \times 10^9$ Ω). (b) I_{SC} of the CF-TENG with different air gap thicknesses ($H = 10$ mm and 100 mm), and the magnitude and phase of the corresponding Fourier series coefficients. (c) The steady-state, transient-state and complete responses of the CF-TENG with an air gap thickness of 10 mm under different loading conditions. (d) Responses of the first and third harmonic under $R_3 = 5 \times 10^9$ Ω.

In section 2.2, it has proved that Norton's equivalent circuit model of a TENG device is equivalent to a time-variant current source connected in parallel with a pure capacitive impedance. The capacitor current ($I_{D,C}$) and resistor current (I_L) of the CF-TENG at different loading resistances ($R_1 = 5 \times 10^8$ Ω, $R_2 = 1.65 \times 10^9$ Ω, $R_3 = 5 \times 10^9$ Ω) are obtained through solving equation (6), and the numerical results are shown in figure 4. It is easily observed that $I_{D,C}$ is phase-leading compared with that of the source current (I_{SC}); and its magnitude increases gradually close to the I_{SC} as the external resistor increases (figure 4(a1)). Conversely, the conduction current (I_L) becomes phase-lagging, but its magnitude is almost similar to the I_{SC} for a small external resistor ($R_1 = 5 \times 10^8$ Ω, figure 4(a2)), and substantially different compared to $I_{D,C}$.

This is because the sum of the $I_{D,C}$ and I_L is equal to I_{SC}, while the latter does not change with either the external resistor or the capacitive impedance. As a result, if one of the currents (such as the conduction current passing through the external resistor) increases, the other one (the capacitor current) decreases accordingly; and the opposite is also true. Furthermore, under periodic mechanical external excitations, the output signals of a TENG device are generally non-sinusoidal waveforms, which can be calculated and analyzed through harmonic analysis that we have mentioned earlier.

Take the CF-TENG as an example, the source current I_{SC} at three different thicknesses of the air gap ($H = 10$ mm, $H = 50$ mm and $H = 100$ mm) are depicted in figures 4(b) and S5. Assume there are 49 sampling points uniformly distributed around the time zero ($N = 49$). Based on the properties of discrete-time Fourier coefficients, there are only 49 distinct harmonic signals in the set (equation (8)), and the relevant coefficients are even and real because of the even and real sequences (figure 4(b)). The characteristics of the harmonic components of the I_{SC} are clearly demonstrated in figures 4(b2), (b3), and S5. It is apparent that all the three I_{SC} signals are mainly composed of the first and third harmonics; the magnitude of the third-order harmonic becomes bigger as the H increases, leading to the difficulty of analysis and control of the CF-TENG device. While the phase angles of 0 and $\pm\pi$ in figure 4(b3) indicate that the corresponding Fourier coefficients are real numbers. There are a number of reasons for this phenomenon, but perhaps the most essential is the composite effects of the transferred charges and the total generated electric field strength distribution along with the H (figure S5). When keeping the external excitation frequency invariable, increasing the H will lead to the deviations of transferred charges on the electrodes from symmetry to meet the requirement of equilibrium states, finally affecting the asymmetrical distributions of the total electric field (figure S5). On the other hand, it can be predicted that increasing H will increase the fundamental frequency, but the magnitude and phase of the corresponding Fourier series coefficients are similar to those depicted in figure 5(b), when the moving speed is not changing.

The relaxation time (τ) is another key parameter, which can react and reveal the change of the capacitive impedance directly. As illustrated in figure 4(c), the relaxation time (τ) is defined as the time taken by the transient state value decayed to 1% of its original level, which grows larger as the external resistors increase, meaning that more time is needed to reach the steady-state. This is due primarily to the obstructions caused by the external resistor, which can impede the charges flowing from one electrode to the other one at a limited time. As a result, the potential difference between the electrodes is gradually enhanced and it becomes close to V_{OC} especially for an extremely large resistor. At the same time, the change of the electric flux ($\Delta\Psi$) that passes through the Gaussian surface (such as S1 depicted in figure 3(a)) does not change obviously, which means the relevant displacement current inside CF-TENG can be reached at steady state in a very long transient time (figure 4(a1)). Thus, connecting a large resistor will increase the relaxation time to transfer from a transient

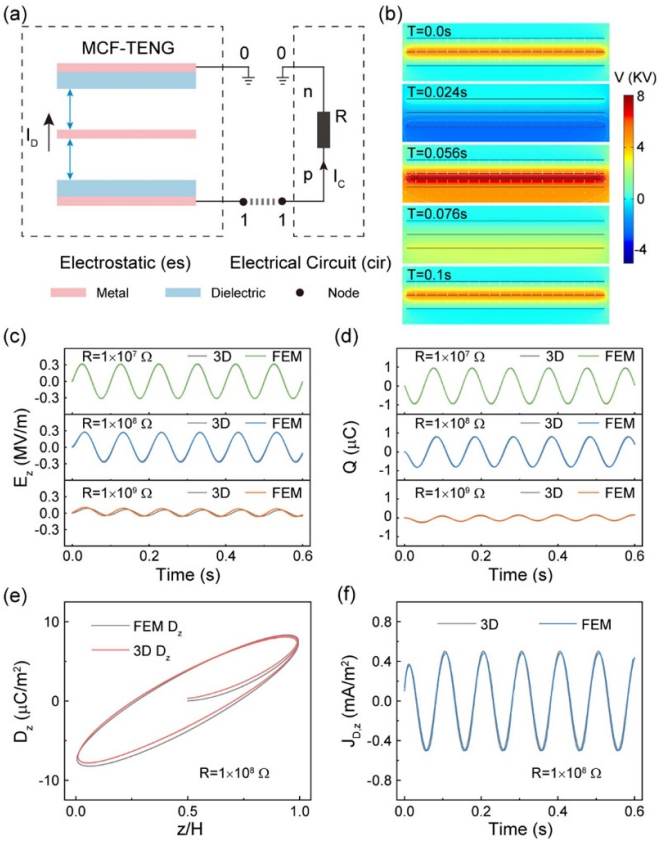

Figure 5. Comparisons of the basic outputs of MCF-TENG from the dynamic simulation model and 3D model. (a) A universal dynamic simulation model for the MCF-TENG. (b) Time-dependent potential in the first cycle simulated using COMSOL Multiphysics software. (c) Variation of E_z in the lower dielectric and (d) transferred charges under three different loads ($R = 10$ MΩ, 100 MΩ, 1 GΩ) versus time. (e) The D_z, and (f) the corresponding displacement current density ($J_{D,z}$) distributed in the lower dielectric layer when $R = 100$ MΩ.

state to steady state not only in the external circuit but also in the internal circuit of the TENG device (figure 4(a1)). Figure 4(d) exhibits the transient, and steady-state responses of the first and third harmonics for a large external resistor ($R_3 = 5 \times 10^9$ Ω) in more detail revealing the transition between states.

According to the theoretical analysis in section 2.3, a dynamic simulation model for the MCF-TENG has been proposed based on the COMSOL Multiphysics software, composed by the electrostatic interface, electrical circuit interface as well as the moving meshinterface (figure 5(a)). This dynamic model can be utilized not only to simulate the physical variables within the TENG device such as the time-varying electric field, electric displacement etc, but also to explore the basic output behavior of the external circuit simultaneously. Most importantly it is a versatile and flexible way of carrying out a dynamic analysis of TENG devices of arbitrary geometry structures and charge distributions. Under a mechanical stimulation and an external connected resistor (detailed parameters shown in table S3 within the supplementary material), the time-dependent potential distribution in the first cycle

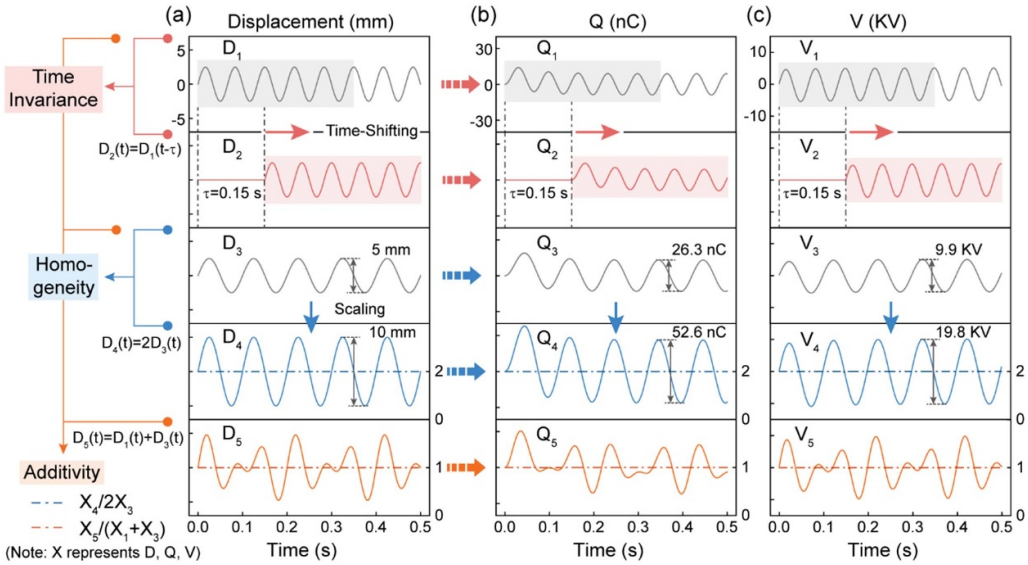

Figure 6. Characteristics of the linearity and time-invariance of the CF-TENG with respect to time. (a) Five different typical mechanical inputs where $D_2(t) = D_1(t-\tau)$, $D_4(t) = 2D_3(t)$, $D_5(t) = D_1(t) + D_3(t)$; (b) the corresponding transferred charges (Q), and (c) the output voltages (V) of the CF-TENG.

of the MCF-TENG is presented in figure 5(b), and the corresponding electric field lines as well as the equipotential lines in six time periods can be observed in the supplementary video. From these results, we can intuitively understand the change of the electric potential and electric field for the geometry structure of the MCF-TENG. The comparisons of electric field, electric displacement, the density of displacement current, and transferred charges under the variation of loading conditions ($R = 10$ MΩ, 100 MΩ, 1 GΩ) are shown in figures 5(c)–(f). The excellent agreement verifies the accuracy of the established dynamic simulation model. Admittedly, compared with the 3D mathematical model of TENGs, the dynamic simulation model makes the energy harvesting system-based TENG device easier to understand and to explain. Furthermore, since COMSOL software is easily realized and has strong analysis capability and powerful pre- and post-processing functions, abundant results can be obtained rapidly and intuitively, which are useful to the design and operation of the TENG device for comparison with industrial applications.

The CF-TENG has some special and useful characteristics that cannot be obtained from other similar models of TENGs. For instance, the V_{OC} and Q_{SC} of the CF-TENG exhibit a linear relationship with the ratio of $\Delta z/H$ with a small thickness of the air gap (figures 2(a) and (b)). And the CF-TENG's capacitance remains constant which is independent of the spatial position of the freestanding layers (figure 2(c)). As a consequence, the energy harvesting system based on the CF-TENG can be modeled as linear time-invariant (LTI) systems. Linearity, that is, superposition, refers to that for an input signal consisting of the weighted sum of several signals, and the output of the system is the weighted sum of the responses of the system corresponding to these signals. The linearity has two-tier meanings: one refers to additivity, the other to homogeneity. Time invariance can be described as a time shift in the input signal resulting in identical time shifts for the output signal. As a result, superposition and time invariance, allows to develop a complete characterization of any LTI system in terms of its response to a unit impulse [21].

For the CF-TENG, at least two requirements should be noticed: (a) the thickness of the air gap should not be too large otherwise the linearity will be destroyed by the non-negligible boundary effect; (b) the starting position of the freestanding layer should be located at the middle point of the air gap. Five different mechanical inputs D_1–D_5 (the expressions for each signal shown in supplementary note 7) and their corresponding transferred charges and output voltage of the CF-TENG are illustrated in figure 6. It is clearly observed that the input signals D_1, D_2 and their corresponding responses directly demonstrate the time invariance characteristic of the CF-TENG. D_2 is defined as D_1 $(t-\tau)$, representing a time-shifted signal, hence it is obvious that various outputs have shown the same time shift τ. D_4 is a scaled signal of D_3 being equal to $2D_3(t)$. Under the mechanical triggering of D_3 and D_4, the transferred charges and output voltages display homogeneity of the CF-TENG exactly. Furthermore, the input signal of $D_5(t)$ is the superposition of D_1 and D_3, that is $D_5(t) = D_1(t) + D_3(t)$. Evidently, these responses are also the superposition of the corresponding responses of D_1 and D_3. The above analysis suggests a theoretical foundation for proposing control strategies and design of hybrid power system towards the engineering application based on CF-TENGs.

The average output power P_{av} and the output efficiency η_{output} are the important physical quantities to estimate the basic output performances of TENGs, because the P_{av} and η_{output} could be utilized to describe the process of energy conversion from different perspectives. The η_{output} is defined by the equation of $\eta_{output} = \frac{E_{load}}{E_{es,av}+E_{load}}$, where E_{load} and $E_{es,av}$ represent the electric energy delivered to the external load and the average quasi-electrostatic energy stored in TENG device during the steady state, respectively. We notice that the maximum

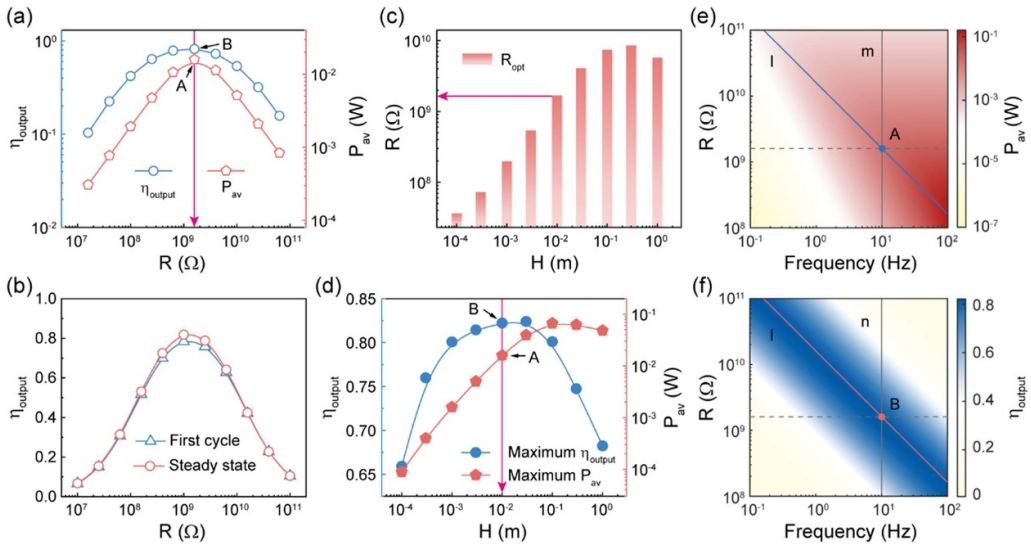

Figure 7. The output efficiency (η_{output}) and average power (P_{av}) of the DCF-TENG under various conditions. (a) The η_{output} and P_{av}, and (b) comparisons of η_{output} from the first cycle and steady state with the 10 mm-thick air gap and 10 Hz frequency at different loading conditions. Variations of (c) the optimum resistance R_{opt} and (d) the maximum of η_{output} and P_{av} versus the thickness of the air gap (H) with a fixed input frequency (10 Hz). The variations of (e) η_{output} and (f) P_{av} with 10 mm-thick air gap at different load resistances and frequencies, respectively. Note that the optimum resistance-frequency relationship is represented by the line *l*.

of P_{av} and η_{output} correspond to the same external resistor which is regarded as the optimum resistance (figure 7(a)). That is because loading a smaller or a larger resistor results in substantial waste energy during the energy transfer process owing to impedance mismatch, which again leads to a decrease in the average power and the output efficiency. The P_{av} and η_{output} obtained from the first cycle are lower than those under steady state, indicating that there is more energy waste at the transient state (figures 7(b) and S6).

The thickness of air gap (H), as an important parameter for the structure, plays a significant role in the energy conversion process, and its influence on the outputs of the DCF-TENG has been studied and shown in figures 7(c) and (d). It is seen that as H increases, the optimum resistance gradually become larger (figure 7(c)), but the corresponding maximum values of P_{av} and η_{output} increase at first but then decrease (figure 7(d)). When the thickness of the air gap is small, lower input mechanical energy is needed, which generates a small amount of transferred charges and electric potential difference between the two electrodes, thus making a small P_{av}. Meanwhile, a large amount of energy is stored in the CF-TENG in the form of quasi-electrostatic energy, and very little electrical energy is outputted, which produces lower η_{output}. However, if the H is too large, the introduced edge effect cannot be ignored [21], which makes P_{av} and η_{output} become smaller again. In order to study the combined effects of the external load resistance and the mechanical frequency, the P_{av} and η_{output} obtained at different loading resistances and frequencies are shown in figures 7(e) and (f). These results confirm our previous discussions and conclusions. Once the structural parameters of the CF-TENG are determined, the corresponding maximum of η_{output} can be determined. For the basic geometry structure of the CF-TENG, the largest η_{output} is obtained and closed to 82.5%.

4. Conclusions

A time-dependent and three-dimensional mathematical model (3D) for the CF-TENGs has been studied starting from a general geometry configuration and charge distributions whereby a solid connection between a physics-based model and dynamic output characteristics is determined. The built mathematical model has a significant advantage in predicting the time-varying output characteristics of TENGs. For the first time, it is confirmed that the signals of transferred charges and electric flux have the same phase as verified from Gauss's theorem. Furthermore, a highly accurate Norton's equivalent circuit model of TENGs is presented based on the capacitive geometry structure of the TENG device, i.e. a combination of a current source and a pure capacitive reactance. Then, not only why the displacement current is the driving force of the TENGs is elucidated, but also the variations of the capacitor current ($I_{D,C}$) and resistor current (I_L) in the internal and external circuit of the CF-TENGs are quantitatively described. It is found that the sum of the $I_{D,C}$ and I_L is equivalent to the source current (I_{SC}), and they are changed in the opposite directions as the increase of the external load resistor, indicating the capacitance characteristics of the TENG device more intuitively.

A universal dynamic simulation model of a TENG device is constructed based on COMSOL Multiphysics software. Using this multiphysics model, one can easily reveal the time-varying physical quantities within the TENGs and the equivalent circuit variables in the external circuit simultaneously. It is worth highlighting that the present model can be expanded to investigate a TENG-based energy harvesting system with arbitrary geometry configurations and charge distributions subject to any external circuit and different conditions. Through the built model, characteristics of the linearity and

time-invariance of the CF-TENG have been validated for five typical mechanical inputs. Finally, we have systematically discussed how the air gap, frequency, and load resistor affect the maximum output average power and output efficiency. We find that the largest output efficiency is close to 82.5%. Universal optimization strategies are suggested to further understand the relationship between physics-based models and practical applications.

5. Methods

The FEM simulations at OC, SC and loading conditions of the CF-TENGs were carried out utilizing COMSOL Multiphysics software. The dynamic simulations couple the electrostatic interface, electrical circuit interface and moving mesh interface together. The distribution of electric potential, electric charge, electric field, electric displacement, displacement current, current and voltage across the external resistors and other physical quantities can be directly obtained from COMSOL software through postprocessing. In addition to FEM simulations, the dynamic results from the 3D model as well as the Norton's equivalent circuit were numerically evaluated using MATLAB (Mathworks Inc.). Details and the parameters utilized in computations and simulations can be found in the supplementary material.

Data availability statement

All data needed to evaluate the conclusions in the paper are present in the paper and/or the supplementary materials. Additional data related to this paper may be requested from the authors.

The data that support the findings of this study are available upon reasonable request from the authors.

Acknowledgments

X Guo and J J Shao contributed equally to this work. Research supported by the National Natural Science Foundation of China (Grant Nos. 62001031, 51702018, and 51432005), National Key R & D Project from Minister of Science and Technology (Grant No. 2016YFA0202704), Fundamental Research Funds for the Central Universities (Grant No. E0E48957), and Youth Innovation Promotion Association, CAS.

Conflict of interest

The authors declare no competing interests.

ORCID iDs

Jiajia Shao https://orcid.org/0000-0002-9777-1930
Morten Willatzen https://orcid.org/0000-0002-8215-9650
Zhong Lin Wang https://orcid.org/0000-0002-5530-0380

References

[1] Wang Z L 2017 On Maxwell's displacement current for energy and sensors: the origin of nanogenerators *Mater. Today* **20** 74–82
[2] Wang Z L 2021 From contact-electrification to triboelectric nanogenerators *Rep. Prog. Phys.* **84** 096502
[3] Shao J J, Liu D, Willatzen M and Wang Z L 2020 Three-dimensional modeling of alternating current triboelectric nanogenerator in the linear sliding mode *Appl. Phys. Rev.* **7** 011405
[4] Shao J J, Willatzen M and Wang Z L 2020 Theoretical modelling of triboelectric nanogenerators (TENGs) *J. Appl. Phys.* **128** 111101
[5] Shao J J, Yang Y, Yang O, Wang J, Willatzen M and Wang Z L 2021 Designing rules and optimization of triboelectric nanogenerator arrays *Adv. Energy Mater.* **11** 2100065
[6] Guo X, Shao J J, Willatzen M, Yang Y and Wang Z L 2022 Theoretical model and optimal output of a cylindrical triboelectric nanogenerator *Nano Energy* **92** 106762
[7] Niu S M, Wang S H, Lin L, Liu Y, Zhou Y S, Hu Y F and Wang Z L 2013 Theoretical study of contact-mode triboelectric nanogenerators as an effective power source *Energy Environ. Sci.* **6** 3576
[8] Dharmasena R D I G, Jayawardena K D G I, Mills C A, Deane J H B, Anguita J V, Dorey R A and Silva S R P 2017 Triboelectric nanogenerators: providing a fundamental framework *Energy Environ. Sci.* **10** 1801
[9] Dharmasena R D I G, Deane J H B and Silva S R P 2018 Nature of power generation and output optimization criteria for triboelectric nanogenerators *Adv. Energy Mater.* **8** 1802190
[10] Niu S M, Zhou Y S, Wang S H, Liu Y, Lin L, Bando Y and Wang Z L 2014 Simulation method for optimizing the performance of an integrated triboelectric nanogenerator energy harvesting system *Nano Energy* **8** 150
[11] Peng J, Kang S D and Snyder G J 2017 Optimization principles and the figure of merit for triboelectric generators *Sci. Adv.* **3** eaap8576
[12] Dharmasena R D I G, Jayawardena K D G I, Mills C A, Dorey R A and Silva S R P 2018 A unified theoretical model for triboelectric nanogenerators *Nano Energy* **48** 391
[13] Shao J J, Willatzen M, Jiang T, Tang W, Chen X, Wang J and Wang Z L 2019 Quantifying the power output and structural figure-of-merits of triboelectric nanogenerators in a charging system starting from the Maxwell's displacement current *Nano Energy* **59** 380–9
[14] Shao J J, Willatzen M, Shi Y and Wang Z L 2019 3D mathematical model of contact-separation and single-electrode mode triboelectric nanogenerators *Nano Energy* **60** 630
[15] Dharmasena R D I G and Silva S R P 2019 Towards optimized triboelectric nanogenerators *Nano Energy* **62** 530–49
[16] Liu W Q and Shi J 2021 A dynamics model of triboelectric nanogenerator transducers *Nano Energy* **89** 106479
[17] Karnopp D C, Rosenberg R C and Margolis D L 2006 *System Dynamics: Modeling and Simulation of Mechatronic Systems* (New York: Wiley)
[18] Zi Y L, Niu S M, Wang J, Wen Z, Tang W and Wang Z L 2015 Standards and figure-of-merits for quantifying the performance of triboelectric nanogenerators *Nat. Commun.* **6** 8376
[19] Deane J H B, Dharmasena R D I G and Gentile G 2018 Power computation for the triboelectric nanogenerator *Nano Energy* **54** 39–49
[20] Lu M Y *et al* 2019 A model for the triboelectric nanogenerator with inductive load and its energy boost potential *Nano Energy* **63** 603883

[21] Niu S M, Liu Y, Chen X Y, Wang S H, Zhou Y S, Lin L, Xie Y N and Wang Z L 2015 Theory of freestanding triboelectric-layer-based nanogenerators *Nano Energy* **12** 769–74
[22] Jiang T, Chen X Y, Han C B, Tang W and Wang Z L 2015 Theoretical study of rotary freestanding triboelectric nanogenerators *Adv. Funct. Mater.* **5** 2928–38
[23] Wang S H, Xie Y N, Niu S M, Lin L and Wang Z L 2014 Freestanding triboelectric-layer based nanogenerators for harvesting energy from a moving object or human motion in contact and non-contact modes *Adv. Mater.* **26** 2818–24
[24] Oppenheim A V, Willsky A S and Nawab S H 1997 *Signals and Systems* (Upper Saddle River, NJ: Prentice-Hall)
[25] Wang Z L 2014 Triboelectric nanogenerators as new energy technology and self-powered sensors—principles, problems and perspectives *Faraday Discuss.* **176** 447
[26] Ghasemi H, Park H S and Rabczuk T 2017 A level-set based IGA formulation for topology optimization of flexoelectric materials *Comput. Methods Appl. Mech. Eng.* **313** 239–58
[27] Ghasemi H, Park H S and Rabczuk T 2018 A multi-material level set-based topology optimization of flexoelectric composites *Comput. Methods Appl. Mech. Eng.* **332** 47–62
[28] Svoboda J A and Dorf R C 2013 *Introduction to Electric Circuits* (New York: Wiley)
[29] Vasandani P, Mao Z-H, Jia W Y and Sun M G 2016 Design of simulation experiments to predict triboelectric generator output using structural parameters *Simul. Model. Pract. Theory* **68** 95–107
[30] Zhang Z N, Yin N, Wu Z S, Pan S H and Wang D A 2021 Research methods of contact electrification: theoretical simulation and experiment *Nano Energy* **79** 105501